Characterizing oxidation, thickness, and composition of metallic glass thin films with combined electron probe microanalysis and X-ray photoelectron spectroscopy

Sachin V. Muley [a, b, *], William O. Nachlas [c, *], Aurelien Moy [c], Paul M. Voyles [a], John H. Fournelle [c]

[a] Department of Materials Science and Engineering, University of Wisconsin-Madison, 1509 University Avenue, Madison, WI 53706, United States of America

[b] Present address – Intel Corporation, 2501 NE Century Ave, Hillsboro, OR 97124, United States of America

[c] Department of Geoscience, University of Wisconsin-Madison, 1215 West Dayton Street, Madison, WI 53706, United States of America

Author contact information:

Sachin Muley (sachinmul@gmail.com, +1-608-422-2165, corresponding author)

William Nachlas (nachlas@wisc.edu, +1-608-262-7964, corresponding author)

Aurelien Moy (amoy6@wisc.edu)

Paul Voyles (paul.voyles@wisc.edu)

John Fournelle (johnf@geology.wisc.edu)

Abstract

Metallic glass thin films (MGTFs) are a recently developed class of alloy coatings with potential applications ranging from biomedical devices to electrical components. Their tribological performance in service conditions is dictated by MGTF bulk composition but can be limited by the native oxide surface that inevitably forms upon exposure to atmosphere. Surface oxidation, thickness, and composition of ZrCuNiAl MGTFs were characterized using a combination of X-ray photoelectron microscopy (XPS) and electron probe microanalysis (EPMA). MGTF samples with nominal thicknesses of 50, 500, and 1500 nm were sputtered onto Si and SiN wafer substrates within a high vacuum deposition chamber and their amorphicity was confirmed by X-ray diffraction. XPS depth profiling identified the thin film composition and showed that the surface oxide was dominated by a mixed layer of mostly ZrO_2, a little oxidized Al, and some metallic Zr. EPMA X-ray intensities were acquired as a function of beam energy to excite characteristic X-rays from different depths of the MGTFs and reconstructed using open-source thin film analysis software *BadgerFilm*, to determine the composition and thickness of sample layers. EPMA results constrain the composition to be $Zr_{54}Cu_{29}Al_{10}Ni_7$ within 0.7 at. % variation and total thicknesses to be 49, 470, and 1546 nm. Using the oxide composition identified from XPS depth profiling as an input for *BadgerFilm* analysis, EPMA results indicate the surface oxidation layer on each of the thin film samples was 6.5 ± 1.1 nm thick and uniform across a 0.25 mm region of the film.

Keywords – metallic glass thin film, composition, electron probe, microanalysis, x-ray photoelectron spectroscopy

1. Introduction

Thin film coatings offer tremendous technological applications in modern life including electronic devices, magnetic recording media, optical coatings, coated cutting tools, and others. Metallic glass thin films (MGTFs) are a recently developed alternative to conventional alloy thin films that exhibit several unique material properties that are beneficial in applications from biomedical devices to electrical components [1]. The surface of MGTFs is characterized by ultra-low coefficient of friction, and combined with Zr-based MGTFs' biocompatibility, makes them an advantageous coating material for minimally invasive surgical devices and syringes [2].

The glass research community continues to demonstrate consistent interest in uncovering structure-property interrelationships in MGTFs to aid their rapid commercialization [3–9]. Driven by the size mismatch in individual atomic sizes, concrete evidence exists for interconnected atomic clusters strongly influencing mechanical and thermal properties in metallic glasses, both in bulk and thin film forms [7,10–13]. In turn, the emergence of key interconnected atomic clusters is shown to depend on alloy composition [12,14], creating a strong incentive to accurately characterize MGTF composition and thickness. Recent results have suggested that surface diffusivity plays an important role during MGTF growth [15–17], but the impact of surface composition on diffusivity remains unresolved. Additionally, developing technologically important MGTFs requires careful design considerations: for example, surface oxidation affects wear performance [18–20], but can improve superelasticity [21], and will ultimately prove decisive to long-term utility of Zr-based MGTFs in biomedical applications. Various thin film composition measurement techniques exist [22–25] and improvements in their accuracy, scope, and applications continue to attract scientific interest. Therefore, development of specialized

characterization tools to evaluate the composition and structure of multi-layered MGTF materials and their surface oxidation will benefit the glass community and other thin film applications.

Electron probe microanalysis (EPMA) is a versatile technique for non-destructive elemental microanalysis of bulk specimens [26]. An electron beam focused onto sub-micron locations of the samples surface is used to excite characteristic X-rays which are then detected with wavelength dispersive X-ray spectrometers (WDS) [26]. EPMA uses diffraction crystal monochromators to selectively diffract X-rays of characteristic wavelength from thin film samples and high purity standards. Chemical composition is then calculated from the ratio of characteristic X-ray intensities from samples and bulk standards and corrected for matrix effects using a matrix correction procedure [27].

Owing to excellent X-ray peak resolution and signal-to-noise ratio together with use of calibration standards, EPMA-WDS can produce precise and accurate quantitative measurements of microvolumes of solid materials. EPMA-WDS is a non-destructive technique that can analyze electrically conductive MGTF samples without surface preparation or coating. EPMA characterization of thin film samples, coated on top of substrates, uses k-ratios (ratio of background corrected X-ray intensity between standard and unknown) acquired at multiple incident beam energies that produce characteristic X-rays from various depths in the sample [28]. Measured k-ratios are compared to theoretical k-ratios calculated from $\phi(\rho z)$ models appropriate to the thin film geometry [29–31]. The thickness and compositions of the thin films and substrate are determined from an iterative calculation scheme that modifies these values until convergence is reached between theoretical and experimental k-ratios. Quantification of thin film thickness and composition can be performed using thin film analysis programs like STRATAGEM, *BadgerFilm* [28,32,33], GMRFilm [34], and PENEPMA [35].

The most recent EPMA quantification methods use models that accurately describe the ionization depth distribution, the so-called phi-rho-Z distribution. Initially designed for bulk sample quantification, these models underwent extensive research in the 1990s to broaden their scope for analyzing layered specimens. Various phi-rho-Z models tailored for thin film analysis, such as PAP, XPP [36], and XPHI [37], have been introduced. Nonetheless, their integration into functional computer programs for routine use in EPMA labs remains limited due to compatibility issues with modern computing systems, limited access behind paywalls, and the high cost associated with acquiring the software license.

To enhance access to thin film analysis tools for EPMA laboratories, *BadgerFilm* — an open-source and freely available software dedicated to thin film analysis – was developed [38]. This open-source software provides a solution to the scarcity of accessible thin film quantification software, thereby facilitating more widespread utilization of such methods within the EPMA community. The software encompasses a simple graphical user interface and integrates the latest $\varphi(\rho z)$ models, along with a non-linear fitting algorithm designed to accurately determine the compositions and thicknesses of complex layered specimens. *BadgerFilm* implements enhanced algorithms for secondary fluorescence calculation [32] which is critical for thin film analysis: in thin film specimens, secondary fluorescence typically represents several percent of the total produced X-ray intensity.

In this work, we show that by combining EPMA experiments and *BadgerFilm* analysis with X-ray photoelectron spectroscopy (XPS), it is possible to perform high-resolution characterization of the composition and thickness of surface oxidation layers of Zr-based MGTFs.

2. Experimental details

Thin film synthesis: Thin films were deposited by employing an in-house built high vacuum direct current magnetron sputtering tool. An arc-melted disc shaped alloy target (diameter 2", thickness 0.125" mounted on copper backing plate of thickness 0.125") with nominal compositions of $Zr_{55}Cu_{30}Al_{10}Ni_5$ (at. %) was commercially acquired from ACI Alloys, CA, U.S.A. The base pressure of the vacuum vessel was better than 1×10^{-7} Torr. The operating pressure of process gas (Ar) was 4.3 mTorr during deposition as measured by a 275i Pirani-style pressure gauge made by Kurt J. Lesker Company. Three suites of thin film samples with nominal composition $Zr_{55}Cu_{30}Al_{10}Ni_5$ were deposited onto Si and SiN substrates and their nominal thicknesses were 50, 500, and 1500 nm. These three suites of thin films were grown at the same direct current sputtering power of 100 W, substrate temperature of 515 ± 3 K using deposition times of 2.5, 20 and 55 min. The deposition rate was nominally estimated to be ~0.43 nm/s, based on characterization from previous studies undertaken on Zr-based alloy systems [7,39]. The MGTF stack had a thin oxide layer atop the much thicker MGTF, all of which sat on top of the underlying Si or SiN substrate. Post deposition, all samples were stored at 22°C in a dry nitrogen (99.9% purity) environment with humidity < 20% that was maintained using silica-based desiccant materials.

Preliminary characterization: A Bruker D8 Discover X-ray diffractometer (XRD) equipped with a Cu-K_α source and area detector was used in the coupled Θ-2Θ setting for structure studies of the thin films. XPS measurements on the 50 and 500 nm thick film samples were performed using a Thermo K alpha X-ray photoelectron spectrometer with monochromatized Al Kα excitation with X-ray spot size of 400 μm and sample spot size of 30 μm. Ar ion gun was used for rapid depth profile to get composition versus depth profiles at discrete etch steps. The change in composition from Zr/Cu/Ni/Al layer to Si substrate was determined based on the XPS depth

profiling data. The etch rate was calculated to be nominally 0.05 nm/s by dividing the film thickness with total etch time through the MGTF to the top of the underlying substrate. The base pressure within the XPS instrument was better than 4×10^{-8} Torr. XPS spectra were analyzed using the manufacturer supplied software package, Avantage v5.9922. In this study, we chose to show the XPS results on 50 nm film grown on Si wafer for clarity of presentation, but the other samples show similar trends.

Compositional analyses using EPMA: EPMA was used to quantify the composition and thickness of thin films and their surface oxidation layer using WDS. A Cameca SX-Five FE-EPMA was used to conduct WDS measurements at 10, 12, 15, 20, 25, and 30 kV accelerating voltage to generate characteristic X-rays from different activation volumes within the sample. At each voltage condition, thirty measurements with spacing 60 μm were acquired from each sample and standard. Analyses were performed with 20 nA beam current and a fully focused beam (~100 nm). X-rays from Zr-Lα (LPET), Cu-Kα (LLIF), Ni-Kα (LLIF), Al-Kα (TAP), Si-Kα (LTAP), and O-Kα (PC0) were collected using five WDS spectrometers equipped with gas flow proportional X-ray detectors. Pure metals were used as calibration standards for Zr, Cu, Ni, Al, and Si. Synthetic Fe_3O_4 was used as calibration standard for O. X-ray intensity for each element was measured at the peak position for 20 seconds and at two off-peak background positions for 10 seconds. A linear interpolation was used for background subtraction of on-peak counts. An exponential background fit was used for O quantification. Differential pulse height analysis was used for Si-Kα on LTAP to account for high order (n=5) reflections from Cu-Kβ.

Figure 1 shows Monte-Carlo simulations of electron beam-specimen interactions within a 500 nm thin film of $Zr_{55}Cu_{30}Ni_5Al_{10}$ atop Si wafer using the Casino (v2.5.1.0) software package [40,41]. By changing primary beam accelerating voltage, it is possible to control the activation

volume from which X-rays are generated. Figure 1 shows the sample volume from which Si-Kα X-rays are generated within this sample geometry at 10 and 25 kV accelerating voltages.

Calculation of thin film thickness and composition: Thin film quantification of MGTF samples and their surface oxidation was performed using *BadgerFilm* (v1.2.11). Experimental k-ratios for each element at every accelerating voltage are used as inputs to extrapolate X-ray emission behavior within thin film and surface oxidation layer. *BadgerFilm* calculates theoretical k-ratios with the PAP phi-rho-z algorithm and modified phi-rho-z matrix correction to determine characteristic and Bremsstrahlung fluorescence effects. The program uses a non-linear fitting algorithm to match calculated k-ratios to experimental k-ratios acquired from a range of accelerating voltages to determine composition and thickness of multi-layered samples. Input parameters include experimental k-ratios from multiple kV conditions, elements present in each layer and material density, standard compositions used to measure k-ratios, and initial guesses for material composition, density, and layer thickness. The program converges on a solution for the composition and thickness of both the MGTF and surface oxidation layer.

BadgerFilm uses k-ratios acquired from multiple accelerating voltages to determine the best-fit parameters for the thickness and compositions of sample layers. *BadgerFilm* uses these parameters to calculate theoretical k-ratios, using phi-rho-Z models, as follows:

$$k_V = \frac{I_{unk;V}}{I_{std;V}}$$

$$= \frac{\sum_{i=0}^{m-1} \int_{\rho z_i}^{\rho z_{i+1}} \phi_i(\rho z; C_1, \dots, C_n; V) e^{-\frac{\mu}{\rho}\Big|_i \frac{\rho z}{\sin\theta}} d\rho z \; e^{-\sum_{j=i}^{0} \frac{\mu}{\rho}\Big|_j \frac{\rho t_j}{\sin\theta}} + \int_{\rho z_m}^{\infty} \phi(\rho z; C_1, \dots, C_n; V) e^{-\frac{\mu}{\rho}\frac{\rho z}{\sin\theta}} d\rho z \; e^{-\sum_{j=m}^{0} \frac{\mu}{\rho}\Big|_j \frac{\rho t_j}{\sin\theta}}}{\int_0^{\infty} \phi_{std}(\rho z; C_1, \dots, C_n; V) e^{-\frac{\mu}{\rho}\Big|_{std} \frac{\rho z}{\sin\theta}} d\rho z}$$

where $I_{unk;V}$ and $I_{std;V}$ are the primary characteristic X-ray intensities emitted by a given element and X-ray line at the accelerating voltage V, from the unknown and the standard, respectively. The

phi-rho-Z distributions for a given characteristic X-ray line and accelerating voltage V, $\phi_i(\rho z; C_1, \ldots, C_n; V)$, are calculated in each thin film i, as well as in the substrate, and are dependent on the concentration of the n elements present in the film (or substrate), C_1, …, C_n. The phi-rho-Z distributions are integrated over the mass thickness, ρt_i, of the ith film: $\rho t_i = \rho z_{i+1} - \rho z_i$, where ρz_i is the mass depth of the ith film. The mass thickness of the substrate is assumed to be infinite. The reabsorption of the emitted characteristic X-rays in the emitting film itself (or substrate) and in the films located above it is considered using the mass absorption coefficient of the film i, $\frac{\mu}{\rho}\Big|_i$. The mass absorption coefficients of the substrate and standard are denoted $\frac{\mu}{\rho}$ and $\frac{\mu}{\rho}\Big|_{std}$, respectively. For more details of the calculation of the theoretical k-ratios and associated phi-rho-Z distributions, as well as for the details of the calculation of secondary fluorescence intensities, see [28,29,32,38].

3. Results and discussion

Preliminary characterization: Figure 2 shows representative structural characterization of the Zr-Cu-Al-Ni thin films (500 and 1500 nm thick; XRD data is not reliable for 50 nm films) by XRD. XRD data confirms amorphous structure of thin films with a first broad diffraction maxima (FBDM) at 37.9° for Zr-Cu-Al-Ni and a second broader maximum at higher angles. The FBDM positions correspond to an average atomic spacing of 0.237 nm in Zr-Cu-Al-Ni. The full width at half maximum (FWHM) has values of 6.4° – 6.9°, depending on the film thickness. Converting the FWHM values to a scattering vector by $q = 4\pi \sin \Theta / \lambda$ (where λ is the X-ray wavelength of the Cu K_α radiation with a value of 1.5418 Å) yield values of ~ 0.45 Å^{-1} – 0.49 Å^{-1}, which are consistent with values reported for Zr-based bulk metallic glasses (~ 0.4 – 0.5 Å^{-1}) [42].

Further structural and microstructural characterization as controlled by deposition parameters is presented elsewhere [39].

Compositional analysis by XPS: Figure 3 shows the survey scan XPS spectra of the 50 nm thick MGTF on Si substrate, both on the surface and within the bulk of the sample after ion etching to a nominal depth of 10 nm. The MGTF surface shows signals for Zr 3s 3p 3d 4s 4p, Al 2s 2p, C 1s, O 1s, very weak Cu 2p, and no Ni 2p peaks. The MGTF bulk shows signals for Zr 3s 3p 3d 4s 4p, Al 2s 2p, Cu 2p, Ni 2p and significantly weaker albeit still present O 1s peaks. O 1s and C 1s peaks show strong presence at the MGTF surface, but C is eliminated by ion etching, and there is a much weaker O signal in the MGTF bulk. Zr, Al, O and C are present in the surface layer, while Ni and Cu are negligible. The MGTF bulk contains Zr, Cu, Al, Ni with a small amount of O.

Figure 4 summarizes depth profiling XPS data with an energy step size of 0.2 eV as a function of ion etching time from zero (film surface) to 240 seconds (~ 10 ± 2 nm) for (a) Zr 3d, (b) Cu 2p, (c) Al 2p, (d) Ni 2p, and (e) O 1s. Near the MGTF surface, XPS spectrum for Zr (Figure 4(a)) shows doublet splitting for both Zr^{4+} and Zr^{0}. At etch levels of 30 s and 60 s, Zr^{4+} doublet splitting happens as Zr $3d_{5/2}$ and Zr $3d_{3/2}$ at 183.7 and 186.1 eV, respectively, while the Zr^{0} doublet splitting happens as Zr $3d_{5/2}$ and Zr $3d_{3/2}$ at 179.2 and 181.6 eV, respectively. The Zr^{4+} doublet peaks indicate presence of ZrO_2. At etch level of 0 s, the Zr oxide doublet peaks are shifted to slightly lower energies, likely due to presence of C as seen in the survey spectrum (Figure 3). As the MGTF is etched beyond 90 s, metallic Zr 3d doublet splitting occurs primarily in the form of Zr $3d_{5/2}$ and Zr $3d_{3/2}$ at 179.2 and 181.6 eV, respectively, with negligible oxide. These results show that Zr exists in the form of mixed oxide and metallic states up to an etch level of 60 s (~3-4 nm

depth) with the oxide content going down as the MGTF is etched over time while being predominantly metallic at etch levels of 90 s and deeper from the MGTF surface.

Figure 4(b) illustrates overlapping Al 2p and Cu 3p spectra as a function of etch time. At etch level of 0 s, we only see a single peak that seems to match with Al^{3+} $2p_{3/2}$ at 75.2 eV with no obvious signals for either Cu or Al in their metallic states. After 30 s of etch time, we see emergence of some Cu^0 $3p_{1/2}$ at 77.6 eV and Cu^0 $3p_{3/2}$ likely overlapped with Al^{3+} $2p_{3/2}$ at 75.4 eV. At 60 s and later etch times, we see emergence of Al^0 $2p_{3/2}$ at 72.3 eV and Ni^0 3p at 66.7 eV in addition to the Cu^0 $3p_{1/2}$ and Cu^0 $3p_{3/2}$ peaks appeared previously. The quantification of Al 2p is especially complicated due to overlap with Cu 3p peaks and is a known issue in XPS quantification of Al-Cu systems [43], but still provides valuable insight into evolution of Al and Cu peaks with etching.

Figures 4(c) and (d) show evolution of Cu 2p and Ni 2p peaks with etch time, respectively. Both Cu and Ni are negligible at 0 s etch step (i.e., at the oxidized film surface). As the MGTF is etched for 30s and later etch times, Cu 2p shows Cu^0 $2p_{3/2}$ and Cu^0 $2p_{1/2}$ at 933.1 eV and 952.9 eV respectively. Similarly, at etch times of 30 s and later, Ni shows Ni^0 $2p_{3/2}$ and Ni^0 $2p_{1/2}$ at 853.1 eV and 870.4 eV, respectively. Cu and Ni emerge in their metallic states fully at 90 s and 120 s etch times, respectively.

Figure 4(e) represents O 1s spectra evolution as MGTF is progressively etched. At 0 s etch level, we see a main peak at ~ 531 eV and a shoulder peak at ~ 532.9 eV corresponding to metallic oxide (OM) and hydroxylated groups (OH), respectively. Taken together with surface states of Zr and Al, our observations indicate the MGTF surface is dominated by mostly ZrO_2 and some Al_2O_3, while the C is likely present in a hydroxylated form leading to the shoulder peak. OM peaks are known to exist at 528 – 531 eV. At etch times of 60 s and later, we see the O 1s peak is ~531 eV

indicating OM peak and the intensity goes down quickly at 90 s and later etch steps. This suggests a very small amount of O at each etch level. The O is assumed to originate from practically immediate oxidation of the freshly etched surface as the XPS instrument is acquired scans over several minutes.

Our findings are broadly consistent with previous XPS depth profiling measurements on Zr-based bulk alloy as well as thin film samples of similar compositions [44–47]. We found the surface oxide layer was mostly composed of ZrO_2, some Al_2O_3 and metallic Zr, adventitious C, and negligible Ni and Cu. This result seems reasonable since Al and Zr are known oxygen getters and have been shown to migrate to the surface and preferentially oxidize in Zr-Cu-Al-Ni alloys [44–47]. Below a nominal film depth of ~3-4 nm, oxide content decreased dramatically, and the film bulk was composed of Zr, Cu, Al, and Ni. The oxide thickness determined by XPS analysis is not expected to be accurate for two reasons: First, the XPS data was acquired periodically at discrete step times meaning it is impossible to pinpoint the exact transition from oxide layer to MGTF and MGTF to underlying substrate. Second, the etch rate estimate does not account for different etch rates of the Zr/Al oxide and the ZrCuAlNi MGTF. However, the XPS analysis confirms the native oxide layer is a few nanometers thick and is dominated by mostly ZrO_2 together with some Al_2O_3 and metallic Zr, consistent with previous reports [44–47].

Other researchers have previously offset the entire XPS spectra to match C 1s peak to 284.6 eV as a calibration technique [44], but this method is considered unreliable for several reasons [48,49]. From the as-acquired spectra, as noted in Fig.4, we found all metal peaks coincided with known metallic and oxide states within reasonable experimental error. This is an expected observation since the metallic sample is held down by copper clips in the XPS setup, making grounding of the surface reliable. Further, we found the adventitious C 1s peak occurred at 286.1

eV, which matches with C-O-C bonding chemistry of C to Al_2O_3 surface according to the XPS instrument manufacturer [50]. Therefore, we did not shift our spectra and have analyzed them as acquired.

Compositional analysis by EPMA: EPMA data were acquired with increasing accelerating voltage to produce characteristic X-rays from progressively greater depths within the sample. We found similar compositional results on films grown on both Si and SiN substrates, so only results for MGTFs grown on the Si substrate are presented in detail here. Figure 5 summarizes raw k-ratios for (a) Zr, (b) Cu, (c) Al, (d) Ni, (e) O, and (f) Si acquired from 50, 500, and 1500 nm thick ZrCuNiAl films. Results from the MGTF samples show that X-ray intensities for all elements decrease with increasing accelerating voltage (Figure 5(a) – (e)) except for Si, which increases with voltage (Figure 5(f)). The raw X-ray intensities (deadtime and background corrected) are converted to k-ratios by analyzing primary bulk standards in parallel at each voltage condition. The increased activation volume at higher kV generates a larger proportion of X-rays from the substrate relative to the thin films. At low kV, Si k-ratios close to zero indicate minimal interaction with the substrate for nominally 500 and 1500 nm MGTF samples. Zr k-ratios are highest at low kV, where most of the signal is coming from the thin film, and progressively decrease with increasing kV. Measured k-ratios for O decrease with increasing voltage initially up to 15 kV, and then plateau at higher voltages. Measure k-ratios for O are independent of MGTF sample thickness for the two thicker samples (i.e., 500 and 1500 nm film thickness).

K-ratios were used to calculate composition and thickness of the sample layers using *BadgerFilm* software [28,29,32,38]. *BadgerFilm* was iterated on the elemental concentrations and films thicknesses (or mass thicknesses) until calculated theoretical k-ratios match experimental k-ratios. The composition of the oxide layer in the *BadgerFilm* model was assumed to be ZrO_2 based

on XPS results, and initial guesses for thickness of the oxide layer, thickness of the MGTF layer, and composition of the MGTF layer were used as input parameters to calculate thickness and composition that match experimental results. The uncertainties given by *BadgerFilm* for the thicknesses and compositions are based on the standard deviations of the experimental k-ratios, which were assumed to be 5%. These standard deviations are used by the non-linear fitting algorithm implemented in *BadgerFilm* to iterate on the parameters, namely composition and thickness, until convergence criteria are met.

Figure 6 shows evaluation of experimental data (solid symbols) with model results from *BadgerFilm* (linear fits) for (a) 50 nm, (b) 500 nm and (c) 1500 nm MGTFs. MGTF composition was calculated to be $Zr_{54}Cu_{29}Al_{10}Ni_7$, indicating close agreement with the starting alloy composition of $Zr_{55}Cu_{30}Al_{10}Ni_5$. The calculations showed small variations of up to 0.7 % in the final compositions across the three samples (Table 1). Further, we acquired transects of EPMA measurements with 20 μm spacing between neighboring points, up to a total distance of 250 μm, to evaluate variability in thickness of MGTF and oxide layer from each of the samples (Figure 7). Calculated thicknesses of 50 nm (Figure 7(a)) and 500 nm (Figure 7(b)) MGTF layers generally agree with the nominal values but show more variability in the 1500 nm sample. Large uncertainties in the calculated thickness of the nominally 1500 nm sample result from very low Si X-ray counts emitted from the substrate. Even at the highest accelerating voltages, the Si k-ratios are very low (0.01 - 0.02) resulting in large uncertainties in the thickness determination. The thickness of the ZrO_2 layer is nearly the same for the three samples and was determined to range from 5.4 to 7.6 nm, represented in Figure 7(c). The errors for data presented in Fig. 7 and Table 1 arise from uncertainties in the input experimental k-ratio measurements which are not related to matrix correction uncertainties and propagated through the fitting algorithm. They do not include any uncertainties from the

phi-rho-Z model or other atomic parameters used to calculate the film thickness and composition. Thus, these error bars can be summarized as reflecting analytical uncertainty of the k-ratio measurements i.e. intrinsic uncertainty from the analysis procedure.

Discussion: Thin film analysis results determined by *BadgerFilm* show good agreement with XPS composition data and expected sample thicknesses. Compositional analyses show a surface oxidation layer grew up to a depth of 6.5 ± 1.1 nm under ambient conditions and then stopped growing. The oxidation layer thickness was found to be about the same for the 50, 500 and 1500 nm samples. These observations are supported by previous studies, showing the kinetics of Zr-Cu-Al-Ni oxidation rate at room temperature under ambient conditions is controlled by back diffusion of Ni and Cu [45,46]. EPMA also showed that the high spatial resolution provided by the focused electron beam enabled characterization of fine-scale variations across the surfaces of thin film materials.

We demonstrate that EPMA as a function of voltage with computational analysis using *BadgerFilm* offers some significant advantages for analysis of multilayer thin films compared to other common analysis techniques. As noted by the present study, XPS with ion etching offers composition data as a function of distance from the top surface of the sample similar to the EPMA results. However, calibration of etching time to physical distance requires additional experimentation, and lateral spatial resolution is inferior to EPMA. Cross-sectional transmission electron microscopy (TEM) can analyze structure and composition of thin films, including surface oxide layers. However, TEM requires destructive sample preparation and is considerably more time consuming and expensive than EPMA. TEM also characterizes an extremely limited volume of material, and that volume can only be expanded at substantial effort and expense. In contrast, EPMA can both survey large regions of the sample materials and capture fine-scale variability.

Rutherford backscatter spectrometry offers similar data to EPMA, but the ion accelerator and detectors required by this technique are more expensive than EPMA and not as commonly available. EPMA with *BadgerFilm* provides a straightforward, quantitative, accessible, and non-destructive method to characterize composition and layer thicknesses for systems like MGTFs and their surface oxides.

4. Conclusions

We demonstrate the capability of *BadgerFilm* thin film analysis software to accurately measure compositions and surface oxidation thicknesses of MGTF specimens comprising several layers. X-ray diffraction confirmed the amorphous nature of thin films. XPS showed that the surface oxide layer was composed primarily of ZrO_2, with some Al_2O_3 and metallic Zr, adventitious C, and negligible Ni and Cu. Below a film depth of few nanometers, oxide content decreased dramatically, and the film bulk was composed of Zr, Cu, Al, and Ni. EPMA measurements from nominally 50, 500, and 1500 nm MGTF samples show that X-ray intensities for all elements decrease with increasing accelerating voltage except for Si, which increases with voltage. At low kV, Si k-ratios close to zero indicate minimal interaction with the substrate for nominally 500 and 1500 nm samples. EPMA data processed using *BadgerFilm* constrains the precise atomic composition to be $Zr_{54}Cu_{29}Al_{10}Ni_7$ within 0.7 % and total MGTF thicknesses to be 49, 470, and 1546 nm. Using the oxide composition identified from XPS depth profiling as an input for *BadgerFilm* analysis, EPMA results indicate the thickness of the oxidation layer is approximately 6.5 ± 1.1 nm and uniform across the surface of the sputtered thin film sample. EPMA measurements made as a function of voltage and analyzed quantitatively with *BadgerFilm* provide a fast, nondestructive method to obtain layer compositions and thicknesses for multilayer samples like the MGTFs studied here.

Acknowledgments

This research was supported by the National Science Foundation (NSF) through the University of Wisconsin Materials Research Science and Engineering Center (DMR-1720415). Final editing and manuscript preparation was supported by NSF DMR-2309000. The authors gratefully acknowledge the use of facilities and instruments supported by NSF through the University of Wisconsin MRSEC (DMR-1720415). Instrumentation support by John Jacobs for XPS measurements is highly appreciated. X-ray diffraction measurements by John Sunderland are acknowledged.

Data availability statement

Data and images presented in figures and all the raw data analyzed to produce those plots is available from DOI: 10.6084/m9.figshare.24584826.

Author Contributions

The manuscript was written through contributions of all authors. All authors have given approval to the final version of the manuscript.

References

[1] J.P. Chu, J.S.C. Jang, J.C. Huang, H.S. Chou, Y. Yang, J.C. Ye, Y.C. Wang, J.W. Lee, F.X. Liu, P.K. Liaw, Y.C. Chen, C.M. Lee, C.L. Li, C. Rullyani, Thin film metallic glasses: Unique properties and potential applications, Thin Solid Films. 520 (2012) 5097–5122. doi:10.1016/j.tsf.2012.03.092.

[2] J.P. Chu, C. Yu, Y. Tanatsugu, M. Yasuzawa, Y. Shen, Non-stick syringe needles: Beneficial effects of thin film metallic glass coating, Sci. Rep. 6 (2016) 31847. doi:10.1038/srep31847.

[3] H. Bin Yu, Y. Luo, K. Samwer, Ultrastable metallic glass, Adv. Mater. 25 (2013) 5904–5908. doi:10.1002/adma.201302700.

[4] P. Luo, C.R. Cao, F. Zhu, Y.M. Lv, Y.H. Liu, P. Wen, H.Y. Bai, G. Vaughan, M. di Michiel, B. Ruta, W.H. Wang, Ultrastable metallic glasses formed on cold substrates, Nat. Commun. 9 (2018) 1389. doi:10.1038/s41467-018-03656-4.

[5] Q. Sun, D.M. Miskovic, K. Laws, H. Kong, X. Geng, M. Ferry, Transition towards ultrastable metallic glasses in Zr-based thin films, Appl. Surf. Sci. 533 (2020) 147453. doi:10.1016/j.apsusc.2020.147453.

[6] D.J. Magagnosc, G. Feng, L. Yu, X. Cheng, D.S. Gianola, Isochemical control over structural state and mechanical properties in Pd-based metallic glass by sputter deposition at elevated temperatures, APL Mater. 4 (2016) 086104. doi:10.1063/1.4960388.

[7] S. V. Muley, C. Cao, D. Chatterjee, C. Francis, F.P. Lu, M.D. Ediger, J.H. Perepezko, P.M. Voyles, Varying kinetic stability, icosahedral ordering, and mechanical properties of a model Zr-Cu-Al metallic glass by sputtering, Phys. Rev. Mater. 5 (2021) 033602. doi:10.1103/PhysRevMaterials.5.033602.

[8] Q. Sun, D.M. Miskovic, H. Kong, M. Ferry, Transition from relaxation to rejuvenation in ultrastable metallic glass driven by annealing, Appl. Surf. Sci. 546 (2021) 149048. doi:10.1016/j.apsusc.2021.149048.

[9] Q. Sun, D.M. Miskovic, M. Ferry, Film thickness effect on formation of ultrastable metallic glasses, Mater. Today Phys. 18 (2021) 100370. doi:10.1016/j.mtphys.2021.100370.

[10] D.P.B. Aji, A. Hirata, F. Zhu, L. Pan, K.M. Reddy, S. Song, Y. Liu, T. Fujita, S. Kohara, M. Chen, Ultrastrong and Ultrastable Metallic Glass, ArXiv Prepr. (2013) 1–24. http://arxiv.org/abs/1306.1575.

[11] J. Hwang, Z.H. Melgarejo, Y.E. Kalay, I. Kalay, M.J. Kramer, D.S. Stone, P.M. Voyles, Nanoscale Structure and Structural Relaxation in Zr50Cu45Al5 Bulk Metallic Glass, Phys. Rev. Lett. 108 (2012) 195505. doi:10.1103/PhysRevLett.108.195505.

[12] P. Zhang, J.J. Maldonis, M.F. Besser, M.J. Kramer, P.M. Voyles, Medium-range structure and glass forming ability in Zr–Cu–Al bulk metallic glasses, Acta Mater. 109 (2016) 103–114. doi:10.1016/j.actamat.2016.02.006.

[13] S. Im, Z. Chen, J.M. Johnson, P. Zhao, G.H. Yoo, E.S. Park, Y. Wang, D.A. Muller, J. Hwang, Direct determination of structural heterogeneity in metallic glasses using four-dimensional scanning transmission electron microscopy, Ultramicroscopy. 195 (2018) 189–193. doi:10.1016/j.ultramic.2018.09.005.

[14] Y.Q. Cheng, E. Ma, Atomic-level structure and structure–property relationship in metallic glasses, Prog. Mater. Sci. 56 (2011) 379–473. doi:10.1016/j.pmatsci.2010.12.002.

[15] A. Annamareddy, Y. Li, L. Yu, P.M. Voyles, D. Morgan, Factors correlating to enhanced surface diffusion in metallic glasses, J. Chem. Phys. 154 (2021) 104502. doi:10.1063/5.0039078.

[16] A. Annamareddy, P.M. Voyles, J. Perepezko, D. Morgan, Mechanisms of bulk and surface diffusion in metallic glasses determined from molecular dynamics simulations, Acta Mater. (2021) 116794. doi:10.1016/j.actamat.2021.116794.

[17] Y. Li, A. Annamareddy, D. Morgan, Z. Yu, B. Wang, C. Cao, J.H. Perepezko, M.D. Ediger, P.M. Voyles, L. Yu, Surface Diffusion Is Controlled by Bulk Fragility across All Glass Types, Phys. Rev. Lett. 128 (2022) 075501. doi:10.1103/PhysRevLett.128.075501.

[18] H. Ma, R. Bennewitz, Nanoscale friction and growth of surface oxides on a metallic glass under electrochemical polarization, Tribol. Int. 158 (2021) 106925. doi:10.1016/j.triboint.2021.106925.

[19] W.S. Chae, N.A. Mohd Yusof, K.H. Lee, S.K. Kwan, H.W. Park, J.Z. Jiang, A. Caron, Corrosion effects on the nanotribology of a Ni62Nb38 metallic glass, Appl. Surf. Sci. 573 (2022) 151628. doi:10.1016/j.apsusc.2021.151628.

[20] D.V. Louzguine-Luzgin, M. Ito, S.V. Ketov, A.S. Trifonov, J. Jiang, C.L. Chen, K. Nakajima, Exceptionally high nanoscale wear resistance of a Cu47Zr45Al8 metallic glass with native and artificially grown oxide, Intermetallics. 93 (2018) 312–317. doi:10.1016/j.intermet.2017.10.011.

[21] F. Li, Z. Zhang, H. Liu, W. Zhu, T. Wang, M. Park, J. Zhang, N. Bönninghoff, X. Feng, H. Zhang, J. Luan, J. Wang, X. Liu, T. Chang, J.P. Chu, Y. Lu, Y. Liu, P. Guan, Y. Yang, Oxidation-induced superelasticity in metallic glass nanotubes, Nat. Mater. 23 (2024) 52–57. doi:10.1038/s41563-023-01733-8.

[22] D. Abou-Ras, R. Caballero, C.-H. Fischer, C.A. Kaufmann, I. Lauermann, R. Mainz, H. Mönig, A. Schöpke, C. Stephan, C. Streeck, S. Schorr, A. Eicke, M. Döbeli, B. Gade, J. Hinrichs, T. Nunney, H. Dijkstra, V. Hoffmann, D. Klemm, V. Efimova, A. Bergmaier, G. Dollinger, T. Wirth, W. Unger, A.A. Rockett, A. Perez-Rodriguez, J. Alvarez-Garcia, V. Izquierdo-Roca, T. Schmid, P.-P. Choi, M. Müller, F. Bertram, J. Christen, H. Khatri, R.W. Collins, S. Marsillac, I. Kötschau, Comprehensive Comparison of Various Techniques for the Analysis of Elemental Distributions in Thin Films, Microsc. Microanal. 17 (2011) 728–751. doi:10.1017/S1431927611000523.

[23] A. Pazzaglia, A. Maffini, D. Dellasega, A. Lamperti, M. Passoni, Reference-free evaluation of thin films mass thickness and composition through energy dispersive X-ray spectroscopy, Mater. Charact. 153 (2019) 92–102. doi:10.1016/j.matchar.2019.04.030.

[24] I. Prencipe, D. Dellasega, A. Zani, D. Rizzo, M. Passoni, Energy dispersive x-ray spectroscopy for nanostructured thin film density evaluation, Sci. Technol. Adv. Mater. 16 (2015) 025007. doi:10.1088/1468-6996/16/2/025007.

[25] J. Bünger, S. Richter, M. Torrilhon, A Model for Characteristic X-Ray Emission in Electron Probe Microanalysis Based on the (Filtered) Spherical Harmonic () Method for Electron Transport, Microsc. Microanal. 28 (2022) 454–468. doi:10.1017/S1431927622000083.

[26] X. Llovet, A. Moy, P.T. Pinard, J.H. Fournelle, Reprint of: Electron probe microanalysis: A review of recent developments and applications in materials science and engineering, Prog. Mater. Sci. 120 (2021) 100818. doi:10.1016/j.pmatsci.2021.100818.

[27] J.I. Goldstein, D.E. Newbury, P. Echlin, D.C. Joy, C.E. Lyman, E. Lifshin, L. Sawyer, J.R. Michael, Scanning Electron Microscopy and X-ray Microanalysis, 3rd ed., Springer US, Boston, MA, 2003. doi:10.1007/978-1-4615-0215-9.

[28] A. Moy, J. Fournelle, BadgerFilm: a versatile thin film analysis program for EPMA and more, Microsc. Microanal. 27 (2021) 1658–1660. doi:10.1017/S1431927621006115.

[29] A. Moy, J. Fournelle, ϕ (ρz) Distributions in Bulk and Thin-Film Samples for EPMA. Part 2: BadgerFilm: A New Thin-Film Analysis Program, Microsc. Microanal. 27 (2021) 284–296. doi:10.1017/S1431927620024927.

[30] Y.G. Lavrent'ev, V.N. Korolyuk, L. V. Usova, Second Generation of Correction Methods in Electron Probe X-ray Microanalysis: Approximation Models for Emission Depth Distribution Functions, J. Anal. Chem. 59 (2004) 600–616. doi:10.1023/B:JANC.0000035269.96076.d2.

[31] M.B. Matthews, B. Buse, S.L. Kearns, Electron Probe Microanalysis Through Coated Oxidized Surfaces, Microsc. Microanal. 25 (2019) 1112–1129. doi:10.1017/S1431927619014715.

[32] A. Moy, J. Fournelle, ϕ (ρz) Distributions in Bulk and Thin Film Samples for EPMA. Part 1: A Modified ϕ (ρz) Distribution for Bulk Materials, Including Characteristic and Bremsstrahlung Fluorescence, Microsc. Microanal. 27 (2021) 266–283. doi:10.1017/S1431927620024915.

[33] M.Y. Efremov, E.A. Olson, M. Zhang, L.H. Allen, Glass transition of thin films of poly(2-vinyl pyridine) and poly(methyl methacrylate): Nanocalorimetry measurements, Thermochim. Acta. 403 (2003) 37–41. doi:10.1016/S0040-6031(03)00122-9.

[34] R.A. Waldo, An iteration procedure to calculate film compositions and thicknesses in electron probe microanalysis, in: Microbeam Anal., San Francisco Press, 1988: pp. 310–314. https://scholar.google.com/scholar_lookup?hl=en&publication_year=1988&pages=310-314&author=RA+Waldo&title=Microbeam+Analysis.

[35] X. Llovet, F. Salvat, PENEPMA: a Monte Carlo programme for the simulation of X-ray emission in EPMA, IOP Conf. Ser. Mater. Sci. Eng. 109 (2016) 012009. doi:10.1088/1757-899X/109/1/012009.

[36] J.-L. Pouchou, F. Pichoir, Quantitative Analysis of Homogeneous or Stratified Microvolumes Applying the Model "PAP," in: K.F.J. Heinrich, D.E. Newbury (Eds.), Electron Probe Quant., Springer US, Boston, MA, 1991: pp. 31–75. doi:10.1007/978-1-4899-2617-3_4.

[37] C. Llovet, X. Merlet, Electron Probe Microanalysis of Thin Films and Multilayers Using the Computer Program XFILM, Microsc. Microanal. 16 (2010) 21–32.

[38] A. Moy, J. Fournelle, BadgerFilm: An Open Source Thin Film Analysis Program, Microsc. Microanal. 26 (2020) 496–498. doi:10.1017/S1431927620014853.

[39] S. V. Muley, D. Chatterjee, A. Bickelhaupt, F.P. Lu, C. Zhang, J.H. Perepezko, P.M. Voyles, Fast surface dynamics of metallic glass thin films influence crystallization during deposition, To Be Submitt. (n.d.).

[40] P.H. and R.G. D. Drouin, CASINO: A New Monte Carlo Code in C Language for Electron Beam Interaction - Part II: Tabulated Values of the Mott Cross Section, Scanning. 19 (1997) 20–28.

[41] V.A. and R.G. D. Drouin, A.R.Couture, D. Joly, X. Tastet, CASINO V2.42 - A Fast and

Easy-to-use Modeling Tool for Scanning Electron Microscopy and Microanalysis Users, Scanning. 29 (2007) 92–101.

[42] D. Ma, A.D. Stoica, X.-L. Wang, Power-law scaling and fractal nature of medium-range order in metallic glasses, Nat. Mater. 8 (2009) 30–34. doi:10.1038/nmat2340.

[43] L.B. Hazell, Quantitative XPS analysis of aluminium in the presence of copper, Surf. Interface Anal. 33 (2002) 791–795. doi:10.1002/sia.1455.

[44] H. Chen, J. Cao, X. Song, J. Liu, J. Feng, Characterization, Removal and Evaluation of Oxide Film in the Diffusion Bonding of Zr55Cu30Ni5Al10 Bulk Metallic Glass, J. Mater. Sci. Technol. 30 (2014) 722–730. doi:10.1016/j.jmst.2013.09.020.

[45] A. Dhawan, V. Zaporojtchenko, F. Faupel, S.K. Sharma, Study of air oxidation of amorphous Zr65Cu17.5Ni10Al7.5 by X-ray photoelectron spectroscopy (XPS), J. Mater. Sci. 42 (2007) 9037–9044. doi:10.1007/s10853-007-1819-z.

[46] S.K. Sharma, T. Strunskus, H. Ladebusch, F. Faupel, Surface oxidation of amorphous Zr65Cu17.5Ni10Al7.5 and Zr46.75Ti8.25Cu7.5Ni10Be27.5, Mater. Sci. Eng. A. 304–306 (2001) 747–752. doi:10.1016/S0921-5093(00)01586-0.

[47] R.P. Oleksak, E.B. Hostetler, B.T. Flynn, J.M. McGlone, N.P. Landau, J.F. Wager, W.F. Stickle, G.S. Herman, Thermal oxidation of Zr–Cu–Al–Ni amorphous metal thin films, Thin Solid Films. 595 (2015) 209–213. doi:10.1016/j.tsf.2015.10.080.

[48] G. Greczynski, L. Hultman, The same chemical state of carbon gives rise to two peaks in X-ray photoelectron spectroscopy, Sci. Rep. 11 (2021) 11195. doi:10.1038/s41598-021-90780-9.

[49] G. Greczynski, L. Hultman, C 1s Peak of Adventitious Carbon Aligns to the Vacuum Level: Dire Consequences for Material's Bonding Assignment by Photoelectron Spectroscopy, ChemPhysChem. 18 (2017) 1507–1512. doi:10.1002/cphc.201700126.

[50] Analysis of adventitious carbon XPS spectra, Thermo Fish. Sci. (n.d.). https://www.thermofisher.com/us/en/home/materials-science/learning-center/periodic-table/non-metal/carbon.html.

Figures

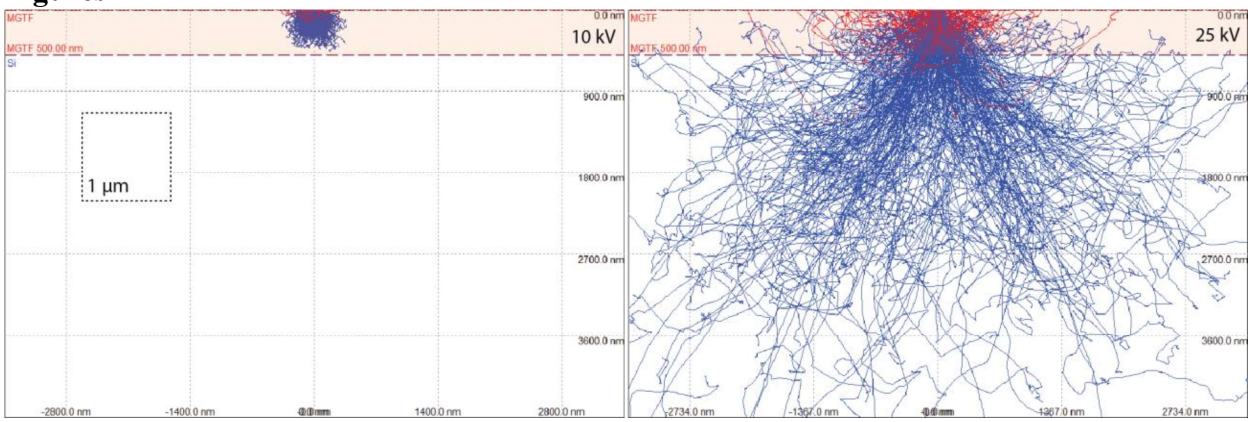

Figure 1: Monte-Carlo simulations using Casino software package of electron-specimen interactions within a 500 nm thin film of $Zr_{55}Cu_{30}Ni_5Al_{10}$ atop Si wafer.

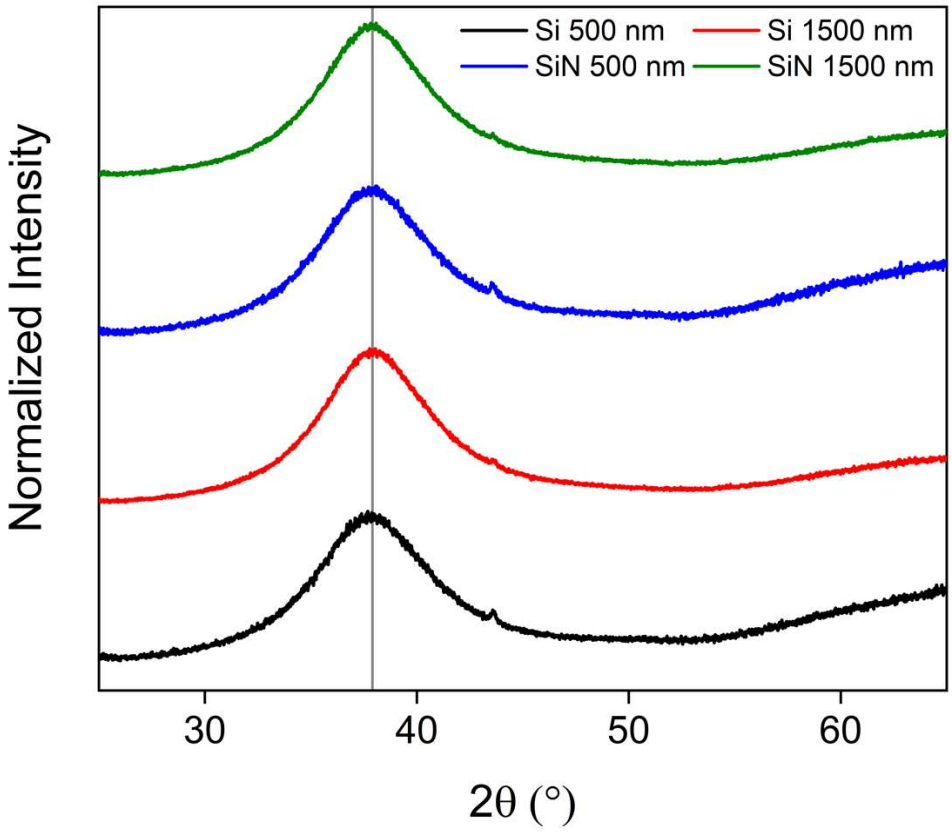

Figure 2: X-ray diffraction results from 500 and 1500 nm thick films grown on both Si and SiN substrates are shown.

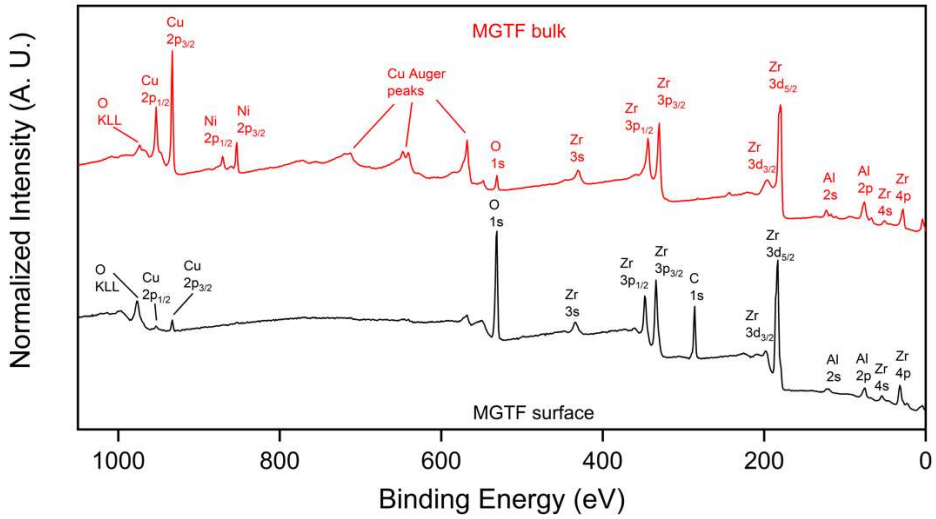

Figure 3: X-ray photoelectron spectrum acquired as part of survey scans on MGTF surface (bottom) and MGTF bulk (top) post ion etching to a nominal depth of 10 nm. Results are shown for MGTF with 50 nm thickness here and were reproducible on 500 nm MGTF as well.

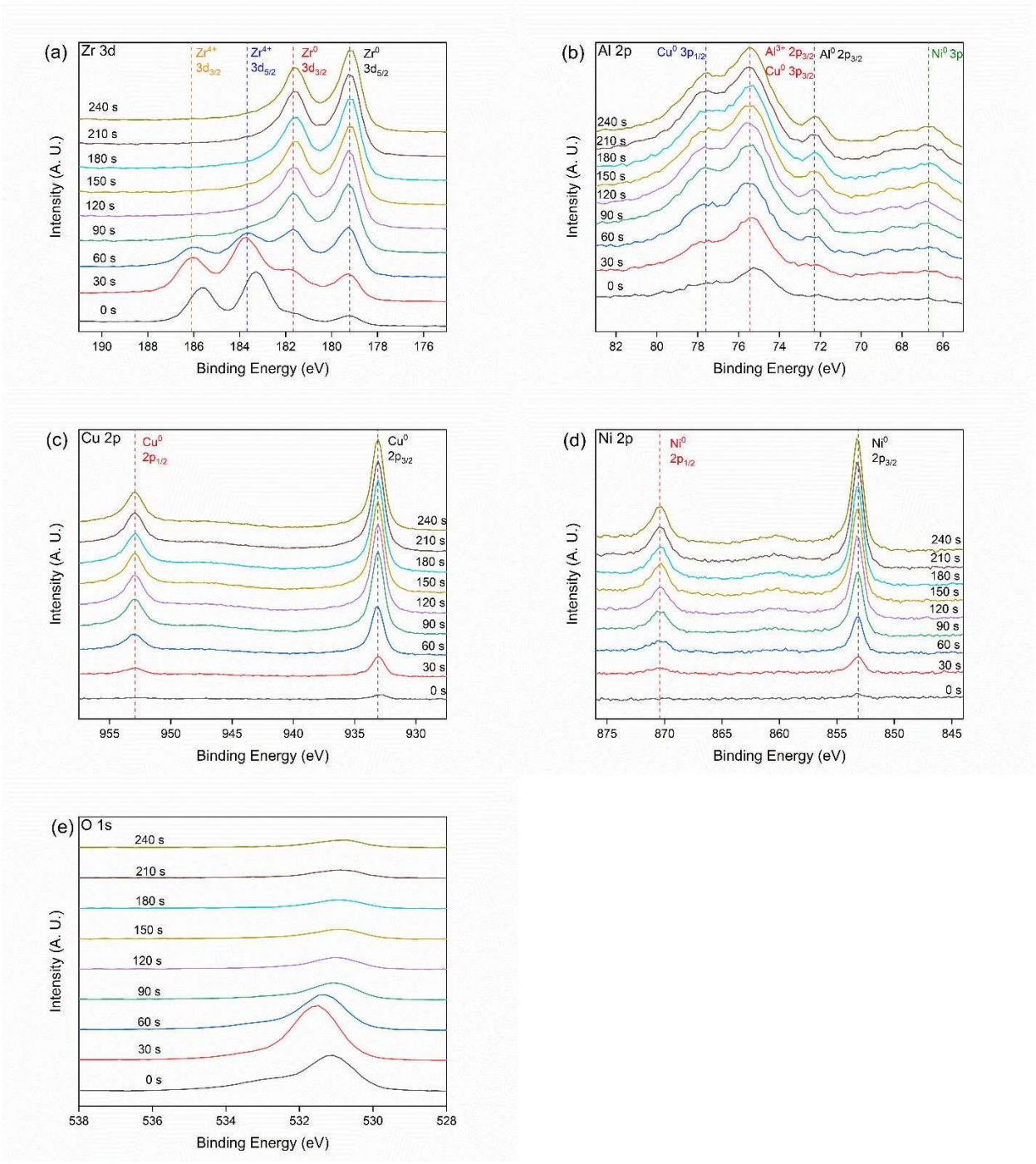

Figure 4: X-ray photoelectron spectrum acquired by ion depth profiling at various etch levels for (a) Zr 3d, (b) Al 2p, (c) Cu 2p, (d) Ni 2p, and (e) O 1s.

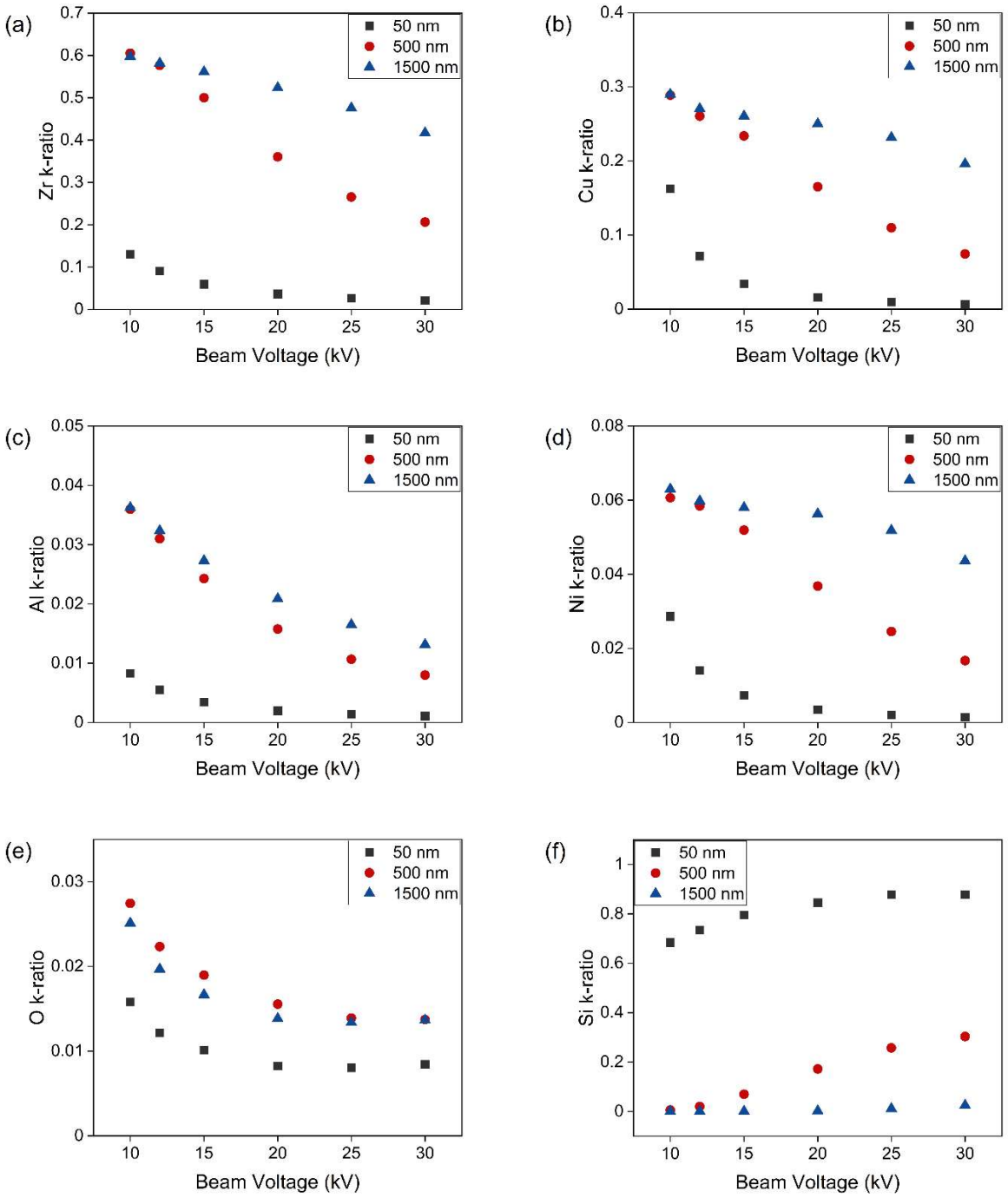

Figure 5: Raw k-ratios for (a) Zr, (b) Cu, (c) Al, (d) Ni, (e) O, and (f) Si acquired from 50, 500, and 1500 nm thick ZrCuNiAl films illustrate the effect of accelerating voltage (kV) on the X-ray intensity emitted from the layers of the samples.

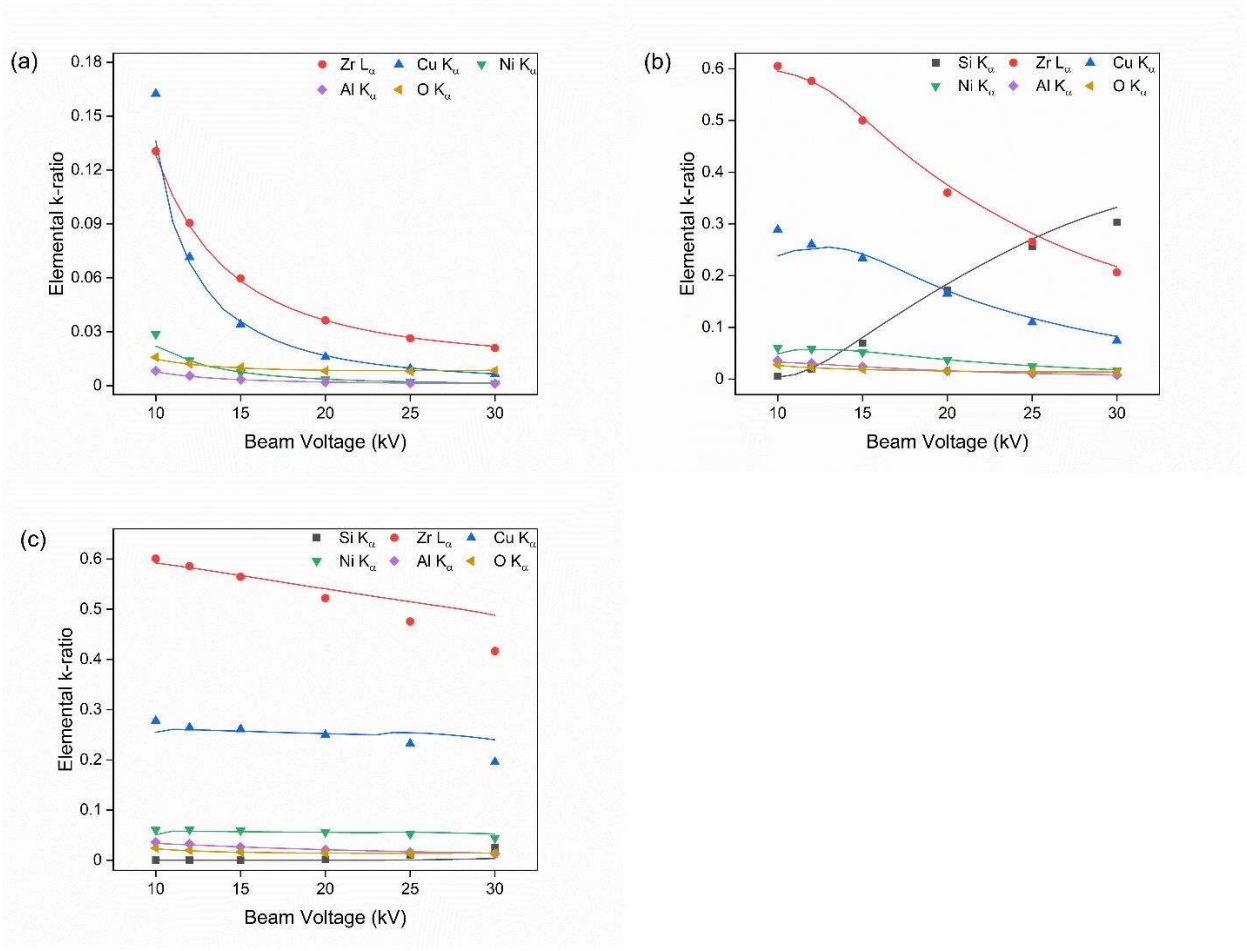

Figure 6: Evaluation of experimental data (solid symbols) with model results from BadgerFilm (linear fits) enable determination of thickness or composition of multi-layered stratified samples for (a) 50 nm, (b) 500 nm and (c) 1500 nm MGTFs.

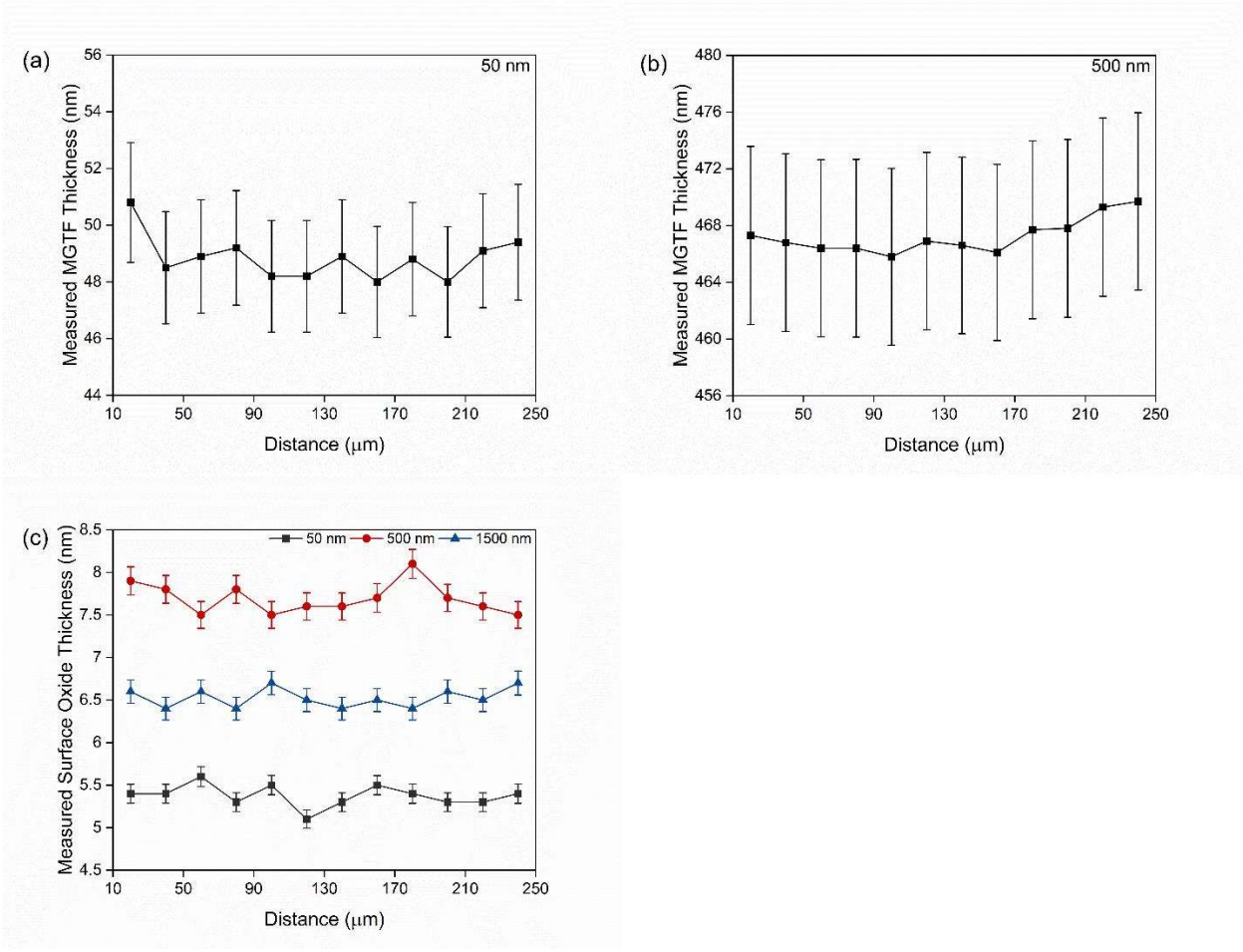

Figure 7: MGTF thickness measured by EPMA of (a) 50 nm, and (b) 500 nm are shown along 250 μm transects. (c) Oxide thickness measured by EPMA on 50 nm, 500 nm, and 1500 nm samples along 250 μm transect are represented.

Tables

Nominal thickness (nm)	MGTF thickness (nm)	MGTF composition (at. %)	Surface oxide thickness (nm)
50	49 ± 2	$Zr_{53.7}Cu_{29.0}Ni_{6.8}Al_{10.6}$	5.4 ± 0.1
500	470 ± 6	$Zr_{53.6}Cu_{29.7}Ni_{6.8}Al_{9.9}$	7.6 ± 0.2
1500	1546 ± 36	$Zr_{53.9}Cu_{29.5}Ni_{6.4}Al_{10.2}$	6.6 ± 0.1

Table 1: Summary of MGTF thickness, composition, and oxide thickness measured by EPMA.